



This is a repository copy of *Functionalized BODIPYs as tailor-made and universal interlayers for efficient and stable organic and perovskite solar cells.*

White Rose Research Online URL for this paper:

<https://eprints.whiterose.ac.uk/196943/>

Version: Accepted Version

Article:

Soultati, A., Nunzi, F., Fakharuddin, A. orcid.org/0000-0001-5589-4265 et al. (22 more authors) (2022) Functionalized BODIPYs as tailor-made and universal interlayers for efficient and stable organic and perovskite solar cells. *Advanced Materials Interfaces*, 9 (21). 2102324. ISSN 2196-7350

<https://doi.org/10.1002/admi.202102324>

This is the peer reviewed version of the following article: Soultati, A., Nunzi, F., Fakharuddin, A., Verykios, A., Armadorou, K. K., Tountas, M., Panagiotakis, S., Polydorou, E., Charisiadis, A., Nikolaou, V., Papadakis, M., Charalambidis, G., Nikoloudakis, E., Yannakopoulou, K., Bao, X., Yang, C., Dunbar, A. D. F., Kymakis, E., Palilis, L. C., Mohd, A. R. B., Argitis, P., Coutsolelos, A. G., De, F., Nazeeruddin, M. K., Vasilopoulou, M., Functionalized BODIPYs as Tailor-Made and Universal Interlayers for Efficient and Stable Organic and Perovskite Solar Cells. *Adv. Mater. Interfaces* 2022, 9, 2102324, which has been published in final form at <https://doi.org/10.1002/admi.202102324>. This article may be used for non-commercial purposes in accordance with Wiley Terms and Conditions for Use of Self-Archived Versions. This article may not be enhanced, enriched or otherwise transformed into a derivative work, without express permission from Wiley or by statutory rights under applicable legislation. Copyright notices must not be removed, obscured or modified. The article must be linked to Wiley's version of record on Wiley Online Library and any reuse, distribution, reproduction or other rights making available the article or pages thereof by third parties from platforms, services and websites other than Wiley Online Library must be prohibited.

Takedown

If you consider content in White Rose Research Online to be in breach of UK law, please notify us by emailing eprints@whiterose.ac.uk including the URL of the record and the reason for the withdrawal request.

Functionalized BODIPYs as tailor-made and universal interlayers for efficient and stable organic and perovskite solar cells

Anastasia Soultati,¹ Francesca Nunzi,^{2,3} Azhar Fakharuddin,⁴ Apostolis Verykios,¹ Konstantina K. Armdorou,⁵ Marinos Tountas,⁶ Stylianos Panagiotakis,¹ Ermioni Polydorou,¹ Asterios Charisiadis,⁷ Vasilis Nikolaou,⁷ Michael Papadakis,⁷ Georgios Charalabidis,⁷ Emmanouil Nikoloudakis,⁷ Konstantina Yanakopoulou,¹ Xichang Bao,⁸ Chunming Yang,⁹ Alan D. F. Dunbar,¹⁰ Emmanuel Kymakis,⁶ Leonidas C. Palilis,¹¹ Abd Rashid Bin Mohd Yusoff,¹² Panagiotis Argitis,¹ Athanassios G. Coutsolelos,^{7,*} Filippo De Angelis,^{2,3,13*} Mohammad Khaja Nazeeruddin,^{14,*} Maria Vasilopoulou^{1,*}

¹Institute of Nanoscience and Nanotechnology, National Center for Scientific Research Demokritos, Agia Paraskevi, 15341 Athens, Greece

²Department of Chemistry, Biology and Biotechnology, University of Perugia, Via Elce di Sotto 8, 06123 Perugia, Italy

³Computational Laboratory for Hybrid/Organic Photovoltaics (CLHYO), Istituto CNR di Scienze e Tecnologie Chimiche (SCITEC-CNR), Via Elce di Sotto 8, 06123 Perugia, Italy

⁴Department of Physics, University of Konstanz, 78457 Konstanz, Germany

⁵Department of Chemistry, National and Kapodestrian University of Athens, 15771, Zografos, Greece

⁶Department of Electrical & Computer Engineering, Hellenic Mediterranean University, Estavromenos, Heraklion, GR-71410, Crete, Greece

⁷Department of Chemistry, University of Crete, Laboratory of Bioinorganic Chemistry, Voutes Campus, Heraklion 70013, Crete, Greece

⁸Qingdao Institute of Bioenergy and Bioprocess Technology, Chinese Academy of Sciences, Qingdao 266101, China

⁹Shanghai Synchrotron Radiation Facility, Shanghai Advanced Research Institute, Chinese Academy of Sciences, Shanghai 201204, China

¹⁰Department of Chemical and Biological Engineering, University of Sheffield, Mappin Street, Sheffield S1 3JD, UK

¹¹Department of Physics, University of Patras, 26 504, Rio, Greece

¹²Department of Chemical Engineering, Pohang University of Science and Technology (POSTECH), Pohang, Gyeongbuk 37673, Republic of Korea

¹³CompuNet, Istituto Italiano di Tecnologia, Via Morego 30, 16163 Genova, Italy

¹⁴Institute of Chemical Sciences and Engineering, École Polytechnique Fédérale de Lausanne (EPFL), Rue de l'Industrie 17, CH-1951 Sion, Switzerland

Abstract

Solar cells based on halide perovskite and polymer donor:non-fullerene acceptor blend absorbers have recently witnessed a significant performance rise. However, they still suffer from some instability issues originating from the inferior interface quality and poor morphology of the absorber layer. In this work, we introduce a series of functionalized boron-dipyrromethene BODIPY molecules as ultra-thin interlayers at the absorber/electron transport layer interface. Our study indicates that appropriately functionalized BODIPY compounds can enhance the device performance mainly due to either a reduction in the work function of the electron transport material upon BODIPY coverage or improvement in the morphology of the absorber layer coated on top of them or both. The best performing devices based on amino-functionalized BODIPY which enabled both of the above effects simultaneously were also proven resistant to degradation when tested upon storage for a long time period or under continuous illumination in nitrogen environment. These results pave the way for the implementation of molecules with tailor-made functionalities in high efficiency and stability solution-based photovoltaics of the future.

1. Introduction

Metal halide perovskite solar cells (PSCs) and organic solar cells (OSCs) are among the best performing solution-processable photovoltaic devices with certified power conversion efficiencies (PCEs) over 25.5% and 19.0%, respectively.^{1,2} They offer added functionalities, *e.g.* transparency, flexibility, aesthetics and solution processability at low temperature making them attractive for

portable and integrated applications and also, in principle, compatible with roll-to-roll production. In both PSCs and OSCs, an absorber layer is employed between a hole transporting layer and an electron transport layer (ETL). In the case of PSCs, the absorber layer consists of halide perovskite, whereas in OSCs it is a mixture of a p-type donor and an n-type acceptor that form a so-called bulk heterojunction (BHJ). For efficient and stable device operation, the quality of the absorber layer and charge transport layers as well as the interfaces between them are of paramount importance.^{3,4}

One such interface is formed between the absorber and the ETL, where the ETL is commonly made of a metal oxide such as titanium, zinc or tin oxide (TiO₂, ZnO, SnO₂).⁵⁻⁷ The surface work function (W_F) of these ETLs needs to be adjusted to the energy levels of the absorber layer for maximum charge extraction and minimum voltage loss.^{8,9} This is why high efficiency PSCs often employ an organic interlayer inserted between the absorber and the ETL. Common interlayer materials include fullerene or non-fullerene acceptors, porphyrin and phthalocyanine derivatives, self-assembled monolayers (SAMs), ionic liquids (ILs) and other organic molecules that modify the W_F while also suppressing interface trap states.^{2,10-14} These interlayers also modify the ETL's surface energy rendering them less hydrophilic, which has a positive influence on the nano-morphology of the absorber overlayer.¹⁵ The surface passivation and better absorber film morphology have a positive influence besides efficiency on the device stability in ambient air, upon heating or under continuous illumination.¹⁶⁻¹⁹ Interlayers to passivate surface defects are also common in OSCs with an inverted architecture using ZnO as the bottom ETL. ZnO forms a reactive interface and, under the presence of UV-light, severely degrades non-fullerene acceptors (NFAs) in the absorber layer through interrupting intramolecular charge transfer (ICT) from the donor to the acceptor segment of these molecules.²⁰⁻²³ As such, range of materials have been employed as interlayers including fullerene derivatives,²⁴⁻²⁶ polymers,^{27,28} SAMs,²⁹ ILs,^{30,31} and many others.³²⁻³⁴ However, there is an inherent limitation regarding the universal application of these interlayers originating from the wide range of ETL/absorber interface properties when changing either the absorber or the ETL or both. A universal

interlayer with a readily synthesized basic molecular structure and easily incorporated tailor-made functionalities is desirable.

The structural diversity of the BODIPY (4,4-difluoro-4-bora-3a,4a-diaza-s-indacene) family provides ample opportunities to easily accomplish and direct structural modification,³⁵ which makes this class of fluorophores especially attractive for application as tailor-made interlayers in PSCs and OSCs. However, to the best of the authors' knowledge, there are no previous reports about their application in both these classes of solar cells. In this work, we perform an extensive study of a series of BODIPY compounds functionalized with various groups such as amino (-NH₂), tertbutyl groups (-C₄H₉), carboxyl (-COOH), hydroxyl (-OH), nitro (-NO₂), ethynyl (-C≡CH), methyl acetate (-COOCH₃) etc., as ultra-thin interlayers between the ETL and the absorber (perovskite or organic BHJ). We verified that these BODIPYs may impact on the device performance and stability (either positively or negatively dependent on the functional group present in each molecule) via a series of theoretical calculations, thin-film measurements and device characterization methods. Among the various compounds tested, BDP-NH₂ demonstrated the highest PCE both in OSCs containing a(poly[(2,6-(4,8-bis(5-(2-ethylhexyl-3-fluoro)thiophen-2-yl)-benzo [1,2-b:4,5-b']dithiophene))-alt-(5,5-(1',3'-di-2-thienyl-5',7'-bis(2-ethylhexyl)benzo[1',2'-c:4',5'-c'] dithiophene-4,8-dione)):(3,9-bis(2-methylene-((3-(1,1-dicyanomethylene)-6,7-difluoro)-indanone))-5,5,11,11-tetrakis(4-hexylphenyl)-dithieno[2,3-d:2',3'-d']-s-indaceno[1,2-b:5,6-b'] dithiophene) (PM6:IT-4F) absorber and PSCs containing methylammonium lead iodide (MAPbI₃). This high PCE was attributed to enhanced electron extraction and improved nano-morphology of the absorber coated on top of it. The universal impact of BDP-NH₂ was further investigated using a highly conjugated NFA acceptor namely 2,2'-((2Z,2'Z)-((12,13-bis(2-ethylhexyl)-3,9-diundecyl-12,13-dihydro-[1,2,5]thiadiazolo[3,4-e]thieno[2'',3'':4',5']thieno[2',3':4,5]pyrrolo[3,2-g]thieno[2',3':4,5]thieno[3,2-b]indole-2,10-diyl)bis(methanylylidene))bis(5,6-difluoro-3-oxo-2,3-dihydro-1H-indene-2,1-diylidene))dimalononitrile (Y6) blended with PM6 (PM6:Y6) in OSCs and a tripple cation Cs_{0.05}FA_{0.8}MA_{0.15}PbI_{2.55}Br_{0.45} perovskite in PSCs, respectively. All these

non-encapsulated devices also demonstrated improved stability under various stress conditions which are typical for device operation, including exposure to ambient environment and continuous illumination with AM 1.5 simulated light in nitrogen without and with simultaneous heating.

2. Results and discussion

2.1 Properties of the interlayers. Functionalized BODIPYs were synthesized and characterized for structural integrity (see Experimental Methods and Fig. S1-S5). Prior to their application device, theoretical studies were performed in order to reveal the optimized geometrical structures (Fig. 1a), energy levels (Table S1), frontier orbitals (Fig. S6), and molecular dipole moments (Table S2). The results clearly show that these materials exhibit quite similar energy levels and energy gap values of nearly 3.0 eV (with the exception of the methyl acetate compound (BDP-COOCH₃), which has an energy gap of 2.2 eV). The electron density in the highest occupied and lowest unoccupied molecular orbitals (HOMO/LUMO) are mostly localized within the BDP unit, except for the nitro compound (BDP-NO₂), the LUMO of which is within the nitro group. However, the calculated molecular dipole moments showed significant variation, ranging from nearly 0.9 D for BDP-NO₂ to 6.67 D for BDP-NH₂, with the vector of this dipole lying mainly on the long molecular axis along the z direction. A high molecular dipole moment as predicted for most of these molecules could be beneficial for device performance, as it might affect interfacial charge transport. This, however, necessitates appropriate molecular orientation so as the dipole moment vector aligns perpendicular to and points towards the ETL substrate.³⁶⁻³⁸

The functionalized BODIPYs were then deposited (via spin-coating from methanol solutions with an optimized concentration of 0.35 mg mL⁻¹ that enabled best device performance) on ZnO which served as the ETL in our OSCs. The BODIPY absorption peaks centered at 475 and 515 nm are hardly distinct in the UV-Vis absorption spectra of BODIPY/ZnO bilayers indicating an ultra-thin nature for the interlayers (Fig. 1b). Exceptions are BDP-OH, BDP-COOH and DTB-pH-BDP where the

formation of thicker BODIPY films on top of ZnO can be concluded from their intense absorption peaks. X-ray photoelectron spectroscopy (XPS) measurements taken in similar BODIPY/ZnO bilayers also indicated the formation of ultra-thin layers in most of the cases (Fig. 1c,d and Fig. S7). XPS spectra exhibit very weak nitrogen (N) and fluorine (F) core level peaks attributed to the expected elements,³⁹ indicating that BODIPYs are present on the ZnO's surface in the form of very thin interlayers. Atomic force microscopy (AFM) images showing the surface topographies of pristine and BODIPY coated ZnO (Fig. S8 a-j) indicated that most of these BODIPYs do not significantly alter the surface topography of ZnO except for BDP-OH, BDP-COOH and DTB-pH-BDP that seem to form aggregated films thus increasing surface roughness. The rest of the BODIPYs mainly filled the "holes" and smoothed the nanostructured surface of ZnO (Fig. S8k,l). It was not possible to estimate the thickness and, especially, the molecular orientation of BODIPYs in the ultra-thin interlayers atop ZnO. Interestingly, the BODIPY covered ZnO layers presented significant differences in water contact angle measurements. Some of them, like BDP-COOH, rendered ZnO's surface more hydrophilic and others, such as BDP-NH₂, rendered it more hydrophobic (Fig. S9). These differences in hydrophobicity will subsequently influence the nano-morphology of the absorber layer deposited on top.

Ultra-violet photoelectron spectroscopy (UPS) measurements (Fig. S10) of pristine and BODIPY coated ZnO films revealed a surface W_F reduction for BODIPYs bearing large molecular dipole moments, such as the tertbutyl- and the amino-functionalized ones where a reduction of 0.3 eV was obtained. On the contrary, the ZnO coated with BDP-NO₂, which exhibits nearly zero dipole moment, presented a W_F similar to the pristine ETL. This is an indication, but not direct experimental evidence of some degree of favorable orientation of these molecules in the interlayers.⁴⁰ It is possible that the functional groups of these BODIPYs are physisorbed onto the ZnO surface resulting in some degree of alignment of their molecular dipole moment vectors along the direction perpendicular to metal oxide and pointing towards the surface. As a result, an interfacial dipole with its negative pole pointing towards ZnO is formed, leading to an electrostatic potential energy change, i.e. reduction of

the ZnO's surface W_F .^{41,42} This can improve electron extraction, thus improving short-circuit current (J_{SC}). However, the formation of a BDP-COOH interlayer resulted in increase of the surface W_F of ZnO despite the fact that this molecule exhibits a significant dipole moment. This could indicate that the molecular dipole moment vector points away from the substrate resulting in the formation of a positive interfacial dipole. Moreover, if the BODIPY is physisorbed onto ZnO with the side of BDP unit and the -COOH group (which is quite hydrophilic) located at the outer surface of modified ZnO substrate this would explain the high hydrophilicity of BDP-COOH/ZnO sample (Fig. S9)

2.2 Performance enhancements in OSCs. To test the hypothesis that ultra-thin BODIPY interlayers of high molecular dipole moment and appropriate molecular alignment might beneficially influence a solar cell performance, we employed these various BODIPYs in OSCs with an inverted device configuration. Prior to device fabrication we confirmed that the BODIPY interlayers were resistant to the organic solvents (chlorobenzene and chloroform) used for the deposition of the organic absorber (Fig. S11). Fig. 2a illustrates the (FTO/ZnO/BDP/PM6:IT-4F/MoO_x/Al) OSC structure and the chemical structures of the PM6 (donor) and the IT-4F (NFA) used in the active layer. In addition, an OSC with pristine ZnO was used as the reference device. The corresponding energy diagram of the fabricated OSCs with either pristine or BODIPY coated ZnO is shown in Fig. 2b. The W_F values of both contacts and the hole transport layer (HTL) (i.e., MoO_x), the valence band maximum of ZnO (pristine and coated with BDPs) and the HOMO and LUMO levels of the polymer donor and NFA were taken from the literature.⁴² The W_F values for pristine ZnO is 3.9 eV, whereas those for ZnO coated with BDPs range between 3.6 and 3.9 eV, except for the ZnO coated with BDP-COOH, which exhibits a W_F of ~4.2 eV. A decrease in the surface W_F of ZnO is generally considered beneficial as it might enhance electron extraction towards the respective electrode. Fig. 2c presents the current density-voltage (J-V) characteristic curves of the best performing PM6:IT-4F-based devices with pristine and different BODIPY-coated ZnO ETLs under simulated AM 1.5 illumination. Table 1 also summarizes the performance characteristics of OSCs based on a PM6:IT-4F absorber using ZnO ETLs with and

without different BODIPY interlayers. We note that the best device performance was obtained when BODIPYs were processed from 0.35 mg mL⁻¹ methanol solutions with only small variations at lower concentrations and when increasing the concentration up to 1 mg mL⁻¹. The device performance significantly declined for higher solution concentrations an indication that the formation of compact BODIPY films might disrupt electron extraction.

Variations in the PCE are observed between the OSCs using the ZnO coated with BODIPYs, with many showing similar or improved device performance compared to the reference device employing pristine ZnO ETL. Exceptions are the devices using DTB-pH-BDP, BDP-COOH and BDP-NO₂ which were always inferior to the reference device. The BDP-NH₂-based OSC exhibited champion device performance, which is due to an increase in J_{SC} (from 20.10 mA cm⁻² to 21.54 mA cm⁻²), V_{OC} (from 0.81 V to 0.87 V), and fill factor (FF) (from 0.68 to 0.74). On overall, a PCE of 13.87 % is attained for BDP-NH₂-based OSC, which is 20 % higher than that of the reference device (11.08 %). Moreover, the BDP-NH₂ devices exhibited high reproducibility, yielding an average PCE of 13.5% (Fig. S12). The series resistance (R_s) for the BDP-NH₂-based device (1.1 Ω cm²) dropped to less than half that of a reference device (2.3 Ω cm², see Table 1). The reduction in R_s reflects the enhanced contact quality of the ETL/absorber interface when ZnO is coated with BDP-NH₂. Fig. 2d shows the external quantum efficiency (EQE) measurements of the fabricated OSCs with and without the BODIPY interlayers. The variation of the EQE values and the calculated J_{SC} are consistent with the J_{SC} of the OSCs based on pristine ZnO and ZnO coated with BODIPYs (Table 1). The charge recombination mechanism in the OSCs with and without BODIPY interlayers was also investigated. Fig. 2e presents logarithmic-linear plots of the variation in measured V_{OC} values for the different devices based on the illumination intensity (ranging between 2 and 100 mW cm⁻²). In the case of DiTetrButyl-BDP, DoH-BDP, BDP-NH₂, and BDP-OH, based OSCs the slopes of V_{OC} decrease from 1.034 kT/q (where k is the Boltzmann constant, q is the elementary charge, and T is the absolute temperature) estimated for the reference cell to nearly unity indicating the suppression of the trap-

assisted recombination losses.^{43,44} On the other hand, higher trap-assisted recombination processes compared with the reference cell occur in the devices with the DTB-pH-BDP, BDP-NO₂, and BDP-COOH indicating poor selectivity of the electron-transporting interface and higher carrier trapping within the organic absorber.

Differences in the nanomorphology of the absorber layer deposited on the different BODIPY modified ZnO samples might be responsible for the variation in recombination losses and overall performance, as it dictates charge transport through the absorber layer. Therefore, the molecular packing and crystallinity properties of absorber films were investigated by grazing incidence wide-angle X-ray scattering (GIWAXS). Fig. 3a and b represent the 1D GIWAXS patterns for the out-of-plane and in-plane directions, respectively, of PM6:IT-4F films coated on ZnO with or without BODIPY interlayers. The PM6:IT-4F layer presents some crystallization in all cases as shown in the in-plane profiles (Fig. 3a), where a diffraction peak at $\sim 0.30 \text{ \AA}^{-1}$, corresponding to a lamellar packing spacing (d) of $\sim 20.9 \text{ \AA}$, appears for all samples. Stronger ring-like lamellar diffraction (100) peaks at $\sim 0.32 \text{ \AA}^{-1}$ ($d: \sim 19.63 \text{ \AA}$) are observed in the out-of-plane direction also suggesting significant crystallinity of the blend films (Fig. 3b). Moreover, a clear π - π stacking diffraction peak can be observed at $q \sim 1.8\text{-}1.85 \text{ \AA}^{-1}$ with a d -spacing distance of $3.49\text{-}3.39 \text{ \AA}$ for all blend films, suggesting preferential face-on orientations with respect to the different ZnO substrates (Table S3). However, there are distinct differences among these samples. For example, a reduced d -spacing of $\sim 19 \text{ \AA}$ is indicated by the shifted lamellar packing diffraction peak at $q \sim 0.33 \text{ \AA}^{-1}$ for the ZnO/BDP-COOH/PM6:IT-4F sample. This implies that BDP-COOH interlayer alters the nanomorphology of PM6:IT-4F on top of it probably due to the high hydrophilicity of the substrate. Further differences between samples were observed in the estimated coherent crystalline length (CCL) for the (100) diffraction peak and π - π stacking direction (010) (Table S3). PM6:IT-4F sample coated on the highly hydrophobic BDP-NH₂/ZnO substrate showed the largest CCL value of $\sim 156 \text{ \AA}$ and 21.65 \AA for the (100) and (010), respectively, an indication of higher crystallinity.⁴⁵ Notably, extremely poor stacking

in the π - π direction was obtained for the DTB-pH-BDP and BDP-NO₂ including samples which explains the inferior device performance and increased trap-assisted recombination in the corresponding devices. The enhancement in crystallinity of the absorber film when deposited on certain BODIPYs-coated ZnO is also related to the slightly improved absorption (Fig. 3c) and reduced overall reflectance (Fig. S13) measured in absorber films (of the same thickness) and complete solar cells, respectively. These along with faster electron extraction indicated by transient photoluminescence (TRPL) measurements (Fig. 3d) can explain both the improved performance of certain devices including BODIPY (i.e., BDP-NH₂) and the inferior efficiencies of the OSCs based on BDP-NO₂, BDP-COOH and DTB-pH-BDP. Potential chemical interactions (i.e., hydrogen bonding coordination) between the BODIPY compounds and the photoactive layer were excluded as a possible explanation for the observed behaviour by conducting proton nuclear magnetic resonance (¹H NMR) titrations in IT-4F:BDP-NH₂ blends (Fig. S14).

We next investigated the long-term stability of the fabricated OSCs using ZnO ETLs with and without the BDP coatings. Fig. 4a shows the variation of PCE versus storage time (in nitrogen) of OSCs using pristine and BDP-coated ETLs (the devices were stored in the dark at room temperature between measurements). The devices employing pristine ZnO ETL and those with DTB-pH-BDP and BDP-NO₂ interlayers showed the highest drop in the PCE values during 100 days of storage with the latter two devices exhibiting significant efficiency losses up to 40% and 60% of the initial PCE, respectively. At the same time, the BDP-NH₂ modified OSC retained nearly 90% of its initial PCE for the same storage time. Furthermore, the photostability of the best performing OSCs based on BDP-NH₂ interlayers was also investigated and compared with that of the reference device. Fig. 4b presents the variation of PCE under continuous AM 1.5 illumination of the OSCs without and with simultaneous heating at 65 °C (the study was performed in nitrogen). Without heating, the BDP-NH₂ device retained nearly 80% of its initial PCE within the 500 h of constant illumination, while the reference device shows a ~40% efficiency drop. Notably, upon heating at 65 °C during illumination,

the BDP-NH₂ based OSC exhibited a nearly 30% efficiency loss whereas the reference device presented severe degradation retaining only 30% of the initial PCE value. The improved stability of the BDP-NH₂-based devices can be related to improvements in the nanomorphology of the photoactive blend and better interface quality.⁴⁶ It can be also attributed to reduced photocatalytic degradation of IT-4F NFA from ZnO upon UV irradiation.²³ This is supported by UV-Vis absorbance and FTIR transmittance measurements of IT-4F coated on ZnO and ZnO/BDP-NH₂ substrates taken when fresh and after continuous illumination with UV light for 10 h (Fig. 4c and d, respectively). No obvious difference in the normalized absorption spectra of fresh IT-4F film coated on ZnO and ZnO/BDP-NH₂ substrates is observed (Fig. 4c). These spectra present strong absorption in the 550-800 nm region with the largest peak at around 720 nm, which is assigned to an ICT from the donor to the acceptor moiety of IT-4F.²³ However, a pronounced photodegradation of the IT-4F film coated on ZnO is indicated by the increased intensity of the shoulder peak at 640 nm compared to the ICT peak at 720 nm.⁴⁷ Prolonged photostability was also evidenced from the fourier-transform infrared (FTIR) spectrum of the illuminated IT-4F deposited on pristine ZnO, compared with the IT-4F deposited on BDP-NH₂ coated ZnO (Fig. 4d). The most obvious difference in the illuminated FTIR transmittance spectra is observed at the range of 1720 cm⁻¹ to 1000 cm⁻¹, where the significant reduction of the main peaks of the NFA upon illumination is evidenced for the ZnO/IT-4F sample. In contrast, a slower photodegradation of IT-4F coated on BDP-NH₂ is observed. The hydrophilic moieties present on the surface of pristine ZnO react during illumination with the carbonyl (C=O) group of IT-4F acceptor, thus destroying its electronic structure and suppressing its ICT ability as evidenced by the above measurements.⁴⁷ A thin BDP-NH₂ interlayer inserted at the NFA/ZnO interface acted as a protective buffer prohibiting the NFA photodegradation. Notably, the UV-Vis absorption spectrum of most of the studied BDPs remained quite stable upon UV light illumination (Fig. S15). This indicates that these compounds are resistant to photodecomposition. Therefore, the small changes of the absorber layer and overall device performance are not related to BODIPYs.

Performance enhancements in PSCs. To test the generality of our approach we next fabricated PSCs with a regular structure (FTO/SnO₂/perovskite/Spiro-MeOTAD/Ag) using a MAPbI₃ absorber and BDP-NH₂ coated SnO₂ ETL. Enhancements in performance metrics (J_{sc}, V_{oc} and FF) were obtained (under reverse scan measurements, Fig. 5a) for the BODIPY device compared to the reference cell. A maximum PCE of 18.78% (average of 18.26%) was obtained for the BDP-NH₂ cell which represents an 11% improvement compared to the reference (where the maximum PCE is 17.0 %, average 15.56%). Notably, a pronounced reduction in the device hysteresis is also observed for the BDP-NH₂ cell (Fig. S16). This performance enhancement was also reflected in the EQE spectra measured in both devices (Fig. 5b). An increase in EQE for the BODIPY cell can be related to the enhanced nanomorphology of the perovskite absorber when spin-coated on the modified ETL (Fig. S17). For the MAPbI₃ film deposited on SnO₂ coated with BDP-NH₂ more compact perovskite films with tightly connected grains of larger size than the reference film are observed. Moreover, enhancement in crystallinity of the perovskite layer coated on the modified ETL is indicated by XRD measurements (Fig. 5c). In particular, more intense and sharper peaks are observed in the XRD diffractogram of MAPbI₃ spin-coated on BDP-NH₂/SnO₂ substrate compared to the reference film. The latter also exhibits a small but distinct peak at around 12.4° an indication of residual PbI₂ from the precursor solution and incomplete transformation to the desired perovskite crystal structure. Additionally, the reduction in steady-state photoluminescence (PL) intensity (Fig. 5c) and faster decay in TRPL measurements (Fig. S18) taken in a perovskite film coated on BDP-NH₂/SnO₂ compared to the reference one suggests improved electron extraction from the perovskite's conduction band into the ETL through the BODIPY coating at the ETL/absorber interface. Furthermore, BDP-NH₂ passivates interface defects of the perovskite layer as evidenced by the increased PL intensity measured in a perovskite film coated on BDP-NH₂/glass compared to the same film coated on bare glass (inset of Fig. 5d).

To explain the passivation effect, we recorded the ^1H NMR spectra of perovskite/BDP-NH₂ mixtures in DMSO-*d*₆ solution. Upon titration with excess MAPbI₃ perovskite solution, all ^1H NMR signals of BDP-NH₂ were almost linearly shielded (Fig. S19) suggesting considerable but non-specific interactions between the molecules in the concentration range studied. Specifically, the chemical shift changes observed for BDP-NH₂ protons are separated into two groups with shielding values of $\sim\Delta\delta=32\text{-}35$ Hz and $\sim\Delta\delta=16$ Hz (Fig. S19a and S20). Reverse titration experiments (Fig. 19b) of MAPbI₃ with BDP-NH₂ solution also showed a nearly linear increase of chemical shift changes (Fig. 19a) but in this case the signals were deshielded (Fig. 5e), reaching a maximum $\Delta\delta=24$ Hz for NH₃⁺. No changes in chemical shifts were detected upon dilution (Fig. S21), suggesting that the BDP-NH₂ molecules do not self-associate by π - π or hydrogen bond interactions. The above observations indicate the presence of molecular interactions between BDP-NH₂ and MAPbI₃ molecules in solution, which are expected to also be present (and potentially strengthened) in thin films, especially if we consider that some of the BDP-NH₂ molecules in the interlayer could be preferentially aligned having their amino- group on the outer surface.

As well as the improvement in efficiency, the PSC stability upon constant illumination without and with heating was also studied. PSCs deposited on top of BDP-NH₂ kept under continuous, simulated 1 sun illumination at 25 °C for 500 h showed a 25% drop from their initial PCE, whereas a 50% efficiency loss is noted for reference cells under the same conditions (Fig. 5f). Moreover, the cell with the BODIPY interlayer maintained nearly 60% of the initial PCE under the combined stresses of thermal heating at 65 °C and 1 sun illumination for 500 h. Under the same measurement conditions, the reference cell exhibited nearly 70% efficiency loss. The better stability of the BDP-NH₂ modified PSCs is also reflected in the absorption spectra and XRD diffractograms (Fig. S22 and S23). On the contrary, the reference films coated on pristine SnO₂ presented significant degradation under continuous illumination. Significant deterioration of the perovskite crystals and formation of PbI₂, which is the result of MAPbI₃ hydrolysis,⁵⁰ is seen for the perovskite films deposited on pristine SnO₂.

The enhanced stability of the perovskite films and complete devices incorporating BDP-NH₂ can be attributed to the passivated interface of the perovskite film when coated on BODIPY.⁵¹ Notably, such films were quite resistant to degradation when exposed to an ambient environment for one year (Fig. S23 and S24).

To further demonstrate the universality of BDP-NH₂ as an example of appropriately functionalized BODIPY for OSCs and PSCs, we fabricated higher efficiency devices by incorporating alternative absorber layers. We employed a highly conjugated NFA within an OSC, namely Y6, that employs a ladder-type electron-deficient-core-based central fused ring (dithienothiophen[3.2-b]-pyrrolobenzothiadiazole) with a benzothiadiazole (BT) core to fine-tune its absorption and electron affinity.⁵² The BDP-NH₂ modified cell showed a champion PCE of 15.69%, significantly higher than the reference cell without the BODIPY interlayer (PCE of 14.01%) (Fig. 6a). This enhancement was also reflected in the increased EQE measured in the BODIPY OSCs (Fig. 6b). Notably, the modified cell was more stable than the reference when subjected to continuous 1 sun AM 1.5 illumination (in nitrogen) without and with simultaneous thermal stress (at 65 °C) (Fig. 6c).

A similar trend in both the device performance (Fig. 6d,e) and stability (Fig. 6f) was also observed in PSCs based on a mixed cation mixed halide Cs_{0.05}FA_{0.8}MA_{0.15}PbI_{2.55}Br_{0.45} perovskite absorber layer.⁵³ With the mixed cation perovskite the BDP-NH₂ device exhibited a champion PCE of 20.12%, significantly higher than the reference cell (PCE of 17.78%). It was also proven to be significantly more resistant to both continuous illumination and heating compared to the reference device. These results demonstrate the beneficial impact of certain BODIPYs when inserted as interlayers between the electron transport material and the absorber in both OSCs and PSCs. In particular, appropriately functionalized molecules such as BDP-NH₂ may be physisorbed with the functional group side facing the ETL substrate thus forcing their molecular dipole moment to be aligned nearly perpendicular and pointing away from the substrate. As a result, a net negative interfacial dipole is formed which reduces the electron extraction barrier. Meanwhile, the BODIPY

segment which is present at the outer surface renders the metal oxide substrate more hydrophobic hence beneficially altering the nano-morphology and crystallinity of the absorber overlayer. However, BODIPYs with other functional groups, such as $-\text{NO}_2$ and $-\text{COOH}$, may disrupt electron extraction or have a negative effect on the nano-morphology of absorber overlayer or both. Therefore, careful design and selection of the BODIPY molecules such that they bear moieties which deliver one or multiple desired functions can further advance the performance of OSC and PSCs.

3. Conclusions

In conclusion, we demonstrated an interfacial engineering approach to fabricate high efficiency and stable PSCs and OSCs through applying functionalized BODIPYs as universal interlayers when deployed at the absorber/ETL interface. The improved performance of devices with appropriate embedded BODIPYs was attributed to a reduction in the electron extraction barrier due to a decrease of the ETL's work function combined with improved nano-morphology/crystallinity of the absorber layer when coated on the BODIPY modified substrate. The optimized devices also demonstrated improved photo- and thermal stability thus confirming the benefits of applying of appropriately functionalized BODIPYs and similar molecules as tailor-made interlayers in solution-based photovoltaics to deliver better power sources in the near future.

4. Experimenta section

Details on the synthetic procedure of BDPs. All reagents and solvents were purchased from usual commercial sources and used without further purification, unless otherwise stated. The ^1H NMR spectra of the BDP compounds were recorded on Bruker AMX-500 MHz and Bruker DPX-300 MHz spectrometers, respectively. The solution of the sample was in deuterated solvent by using the solvent peak as the internal standard. High-resolution mass spectra were recorded on a Bruker ultrafleXtreme

MALDI-TOF spectrometer, using trans-2-[3-(4-tert-butylphenyl)-2-methyl-2-propenylidene] malononitrile as matrix.

Synthesis of 3,5-di-tert-butyl-4-(hexyloxy)benzaldehyde. Potassium carbonate (2.36 g, 17.07 mmol) was added to a solution of 3,5-di-tert-butyl-4-hydroxybenzaldehyde (1 g, 4.27 mmol) in DMF (6 mL) at room temperature. After the mixture had been stirred at 60 °C for 1 h, 1-bromohexane (1.5 mL, 10.67 mmol) was added slowly. The reaction mixture was stirred overnight at 80 °C under N₂. The solvent and the excess of 1-bromohexane were removed under reduced pressure. Water was added to the residue and the product was extracted with ethyl acetate (EtOAc) (2x50 mL). The organic layer was dried over Na₂SO₄ and concentrated in vacuo to give the desired aldehyde as an oily liquid (1.2 g, 90%). ¹H NMR (300 MHz, CDCl₃): δ = 9.90 (s, 1H), 7.78 (s, 1H), 3.65 (t, *J* = 7.7 Hz, 2H), 1.89 (m, 2H), 1.44 (s, 18H), 1.31 (m, 6H), 0.88 (m, 3H) ppm (Fig. S2).

General procedure for the synthesis of BDPs (1-9, Fig. S1). To a 250 mL round-bottomed flask containing 50 mL of dry and degassed CH₂Cl₂, 2,4-dimethylpyrrole (2.3 eq.) and any of the corresponding 4-substituted benzaldehyde (1 eq.). Namely, 3,5-di-tert-butylbenzaldehyde for **1**, 3,5-di-tert-butyl-4-(hexyloxy)benzaldehyde for **2**, 2,6-bis(hexyloxy)benzaldehyde for **3** (1), 4-(prop-2-yn-1-yloxy)benzaldehyde for **4** (2), 4-nitrobenzaldehyde for **5**, 4-formylbenzoic acid for **7**, 4-hydroxybenzaldehyde for **8** and methyl 4-formylbenzoate for **9**. One drop of trifluoroacetic acid (TFA) was added and the solution was stirred under N₂ at room temperature overnight. Then, 1 eq. of tetrachloro-*p*-benzoquinone (p-Chloranil) was added to the reaction mixture and stirred for an additional 30 minutes. Consequently, 2.26 mL of BF₃·OEt₂ and 2.34 mL of Et₃N were successively added and the reaction mixture was stirred for another 6 hours. Upon the reaction completion, the mixture was washed three times with water (3 x 50 mL) and dried over anhydrous Na₂SO₄. The solvent was evaporated and the residue was purified by silica gel column chromatography leading to **1** (30%), **2** (21%), **3** (29%), **4** (25%), **5** (28%), **7** (24%), **8** (26%) and **9** (25%).

For **2**: ^1H NMR (300 MHz, CDCl_3): $\delta = 7.09$ (s, 2H), 5.98 (s, 2H), 3.65 (t, $J = 7.7$ Hz, 2H), 2.55 (s, 6H), 1.86 (m, 2H), 1.58 (m, 2H), 1.40 (m, 24H), 1.35 (m, 4H), 0.91 (m, 3H) ppm (Fig. S3). MS (MALDI-TOF): calculated for $\text{C}_{33}\text{H}_{48}\text{BF}_2\text{N}_2\text{O}$ $[\text{M}+\text{H}]^+$ 537.3828; found 537.3828.

For **3**: ^1H NMR (300 MHz, CDCl_3): $\delta = 7.31$ (t, $J = 8.4$ Hz, 1H), 6.58 (d, $J = 8.3$ Hz, 2H), 5.90 (s, 2H), 3.90 (t, $J = 6.2$ Hz, 4H), 2.53 (s, 6H), 1.57 (m, 4H), 1.51 (s, 6H), 1.14 (m, 12H), 0.79 (m, 6H) ppm (Fig. S4). MS (MALDI-TOF): calculated for $\text{C}_{31}\text{H}_{43}\text{BF}_2\text{N}_2\text{O}_2$ $[\text{M}]^+$ 524.3386; found 524.3378.

For (**6**): A mixture of **5** (0.05 g, 0.135 mmol) in dry THF (30 mL) and dry Et_3N (70 μL) containing 10% Pd/C (0.022 g, 0.22 mmol) was stirred for 3 hours under hydrogen atmosphere at room temperature. Upon completion of the reaction, the resulting mixture was filtered through a Celite pad. The filtrate was collected and evaporated to dryness under reduced pressure. The crude product was then purified by column chromatography (silica gel, CH_2Cl_2) to afford BDP **6** in 80% yield. ^1H NMR (500 MHz, CDCl_3): $\delta = 7.03$ (d, $J = 8.1$ Hz, 2 H), 6.82 (d, $J = 8.1$ Hz, 2 H), 5.97 (s, 2 H), 4.22 (sb, 2 H), 2.54 (s, 6 H), 1.49 (s, 6 H) ppm (Fig. S5). HRMS-(MALDI-TOF): m/z calc. for $[\text{M}]^+$ $\text{C}_{19}\text{H}_{20}\text{BF}_2\text{N}_3$ 339.1718, found 339.1722.

Materials and thin film characterization methods. UV-Vis absorption measurements of the different ESLs with and without absorber films coated on them as well as reflectance measurements of the fabricated OSCs were performed using a Perkin Elmer Lambda 40 spectrometer. For the XPS measurements, the AlK α K α line at 1486.6eV (12kV with 20mA anode current, not monochromized) was used with an analyser (Leybold EA-11) pass energy of 100eV, giving a full width at half maximum (FWHM) of 1.5eV for the Au 4f $_{7/2}$ peak. In all XPS spectra, the binding energy (BE) of the predominant aliphatic contribution of the C 1s peak at 284.8eV was used as a measured BE reference. For the UPS measurements, the He I excitation line (21.2eV) was used, and a negative bias of 12.22V was applied to the specimen in order to separate the high binding energy cut-off from the analyser. A Bruker Tensor 27 FTIR spectrometer with a DTGS detector was used to take FTIR transmittance spectra of the NFA deposited on ZnO with and without BDP coatings. GIWAXS measurements of the

same samples were performed using beamline BL16B1 (Shanghai Synchrotron Radiation Facility). The surface topographies/morphologies of ZnO pristine and coated with BDPs were acquired by a NT-MDT AFM. The crystalline composition of perovskite films were investigated using an X-ray Siemens D-500 606 diffractometer. SEM images of the perovskite films were recorded with a JEOL 7401f FESEM. PL spectra of absorber films used in both organic and perovskite solar cells were taken using a 450 nm laser diode module and a Si photodiode and analyzed with an Oriel 77200 monochromator.

NMR Experiments. ^1H NMR spectra were recorded on a Bruker Avance 500 MHz spectrometer as solutions in deuterated DMSO- d_6 using the residual solvent signal as the internal standard and were processed with Topspin 4.0.8. Solutions of BDPNH₂ in DMSO- d_6 (5.55 mM) diluted at 2.95 mM and a concentrated solution of CH₃NH₃PbI₂ (2.8 M) were prepared. The solution of CH₃NH₃PbI₂ was then added in a small aliquots (10 μL , corresponds to 0.055 M), to reach the final ratio BDP-NH₂/CH₃NH₃PbI₂ from 5% to ~ 0 mol/mol, as used for the preparation of photovoltaic cells. The reverse experiment was also carried out. Solutions of CH₃NH₃PbI₂ (2.8 M) and BDP-NH₂ (stock solution, 69.28 mM) were prepared. The solution with BDPNH₂ was then added in small aliquots (10 μL) to the CH₃NH₃PbI₂ solution until almost the same final ratio as in the forward experiment was reached.

Theoretical calculations. Molecular geometry optimizations were carried out without symmetry constraints at the density functional level of theory, by using Gaussian 09 code employing the B3LYP functional. The standard 6-31+G(d,p) basis set was used.

Fabrication and characterization of OSCs and PSCs. In the case of OSCs, a ZnO ETL was deposited on fluorine-doped tin oxide (FTO)/glass substrates purchased from Solaronix. The FTO/glass substrates were first washed by sonication sequentially in deionized water, acetone, and isopropyl alcohol for 10 minutes each. A thin film (~ 50 nm) of ZnO was applied on the FTO cathode electrode using solution-processing followed by thermal annealing at 250 $^\circ\text{C}$ for 20 minutes. The ZnO film was deposited from a 0.5 Mmol L⁻¹ ZnO sol-gel that was prepared using zinc acetate dihydrate in

a mixture of ethanolamine and 2-methoxyethanol through spin-coating at 6000 rpm for 40 sec. The BODIPYs were spin-coated onto the ZnO ETL to act as interlayer between the absorber and the ETL from a 0.35 mg mL⁻¹ methanol solution at 2000 rpm for 40 sec. The PM6:IT-4F absorber film was spin-coated on top in an argon-filled glovebox at 1000 rpm for 90 s from a 20 mg mL⁻¹ (1:1.2 weight ratio) solution in chloroform (CF) with 0.5 v/v% 1,8-diiodooctane (DIO) as an additive to form uniform films. These were then placed on a hotplate at 100 °C for 10 min (also in the glovebox). PM6:Y6 absorber was processed from a 16 mg mL⁻¹ solution (1:1.2 weight ratio) in CF with 0.5% 1-chloronaphthalene (CN) as an additive. The solution was spin coated (2500-3000 rpm) onto the ZnO layer to obtain a photoactive layer of thickness 100 nm. Next, a hole transport layer (HTL) consisting of MoO_x was deposited on the PM6:IT-4F film with a hot-wire chemical vapor deposition method. To complete the device, an Al top electrode was deposited using a thermal evaporation system, where a shadow mask was used to form an active cell area of 12.56 mm². Organic solar cell electrical characterization was performed using a Keithley 2400 source-measure unit, where the J-V characteristic curves of the fabricated devices were recorded under illumination and in dark conditions. A Xe lamp with an AM 1.5G filter was used as the illumination source. All chemicals were purchased from Ossila except for solvents which were purchased from Sigma-Aldrich.

Fabrication of PSCs. Tin oxide (SnO₂) was purchased from Alfa Aesar. 2,2',7,7'-Tetrakis [N,N-di (4-methoxyphenyl) amino]-9,9'-spirobifluorene (Spiro-MeOTAD), lithium bis(trifluoromethanesulfonyl)imide (Li-TFSI ≥ 99 %), 4-tert-butylpyridine (TBP 96.6 %) were purchased from Sigma Aldrich, while FK209 (FK 209 Co(II) PF6) from GreatCell. The materials for the perovskite layer: PbI₂ and PbBr₂ (99.99% purity) were bought from TCI, and the FAI and MABr were purchased from GreatCell Solar. CsI (99.999%) was purchased from Alfa Aesar and finally RbI (99.8%) was obtained from Sigma-Aldrich. Dimethylformamide (DMF) anhydrous 99.8%, dimethyl sulfoxide (DMSO) anhydrous ≥ 99.9% and chlorobenzene (CB) 99.8% were obtained from Sigma-Aldrich. Toluene 99.7% and isopropanol (IPA) >99.8% were purchased from Honeywell Research

Chemicals.

Regular n-i-p PSCs were fabricated starting from the deposition of SnO₂ on FTO substrates, which were first cleaned with Triton-X, acetone, and 2-propanol followed by oxygen-plasma treatment for 15 min. SnO₂ purchased from Alfa Aesar was diluted in water (1:4) and spin-coated at 3000 rpm for 40 sec. The prepared films were then heated at 150 °C for 30 min. Subsequently, BDPs were spin-coated on SnO₂ from a 0.35 mg mL⁻¹ methanol solution at 2000 rpm for 40 sec. MAPbI₃ was formed using a two-step spin-coating procedure. A 1 M PbI₂ solution was prepared by dissolving 462 mg PbI₂ in 1 mL N,N-dimethylformamide (DMF) under stirring at 70°C. 20 µL of PbI₂ solution was spin-coated on the ETL at 3000 rpm for 5 s and 6000 rpm for 5 s (no loading time). After spinning, the film was dried at 100 °C for 10 min. After cooling to room temperature, 200 µL of 0.044 M MAI solution in 2-propanol was loaded on the PbI₂-coated substrate and allowed to stand for 20 s (loading time) before spinning at 4000 rpm for 20 s and then drying at 100 °C for 5 min. For the Cs_{0.05}FA_{0.8}MA_{0.15}PbI_{2.55}Br_{0.45} precursor solution (1.2 M) was prepared with FAI (0.96 M), MABr (0.18 M), PbI₂ (1.014 M), PbBr₂ (0.186 M), and CsI (0.06 M) dissolved in a mixture of DMSO and DMF (4:1 v/v) for one step spin-coating. 20 µL of (2,2',7,7'-tetrakis(N,N-di-p-methoxyphenylamine)-9,9-spirobifluorene) (Spiro-MeOTAD) solution was spin-coated on the perovskite layer at 4000 rpm for 30 s. The spiro-MeOTAD solution was prepared by dissolving 72.3 mg of Spiro-MeOTAD in 1 mL of chlorobenzene, to which 28.8 µL of 4-tert-butyl pyridine and 17.5 µL of lithium bis(trifluoromethanesulfonyl)imide (Li-TFSI) solution (520 mg LI-TSFI in 1 mL acetonitrile) were added. Finally, 80 nm of silver was thermally evaporated on the Spiro-MeOTAD coated film. J-V characteristics curves of the fabricated PSCs were taken using an Autolab PG-STAT-30 potentiostat (1 sun, 100 mW cm⁻²) including an AM 1.5G filter. The EQE spectra of both OSC and PSC were obtained using an Autolab PG-STAT-30 measurement system using an Oriel 1/8 monochromator and a 300 W Xe lamp, and the light intensity at each wavelength was calibrated with a standard single-crystal Si photovoltaic cell.

Supporting information including Fig. S1-S35, Table S1-S3 and references is available.

Acknowledgement

We acknowledge support of this work by the project “Development of Materials and Devices for Industrial, Health, Environmental and Cultural Applications” (MIS 5002567), which is implemented under the “Action for the Strategic Development on the Research and Technological Sector”, funded by the Operational Programme "Competitiveness, Entrepreneurship and Innovation" (NSRF 2014-2020) and co-financed by Greece and the European Union (European Regional Development Fund). A.S. and M.T. acknowledge the support of this research which is co-financed by Greece and the European Union (European Social Fund- ESF) through the Operational Programme «Human Resources Development, Education and Lifelong Learning» in the context of the project “Reinforcement of Postdoctoral Researchers - 2nd Cycle” (MIS-5033021), implemented by the State Scholarships Foundation (IKY).

References

1. The National Renewable Energy Laboratory, Best Research-Cell Efficiency Chart; www.nrel.gov/pv/cell-efficiency.html.
2. Y. Cui, Y. Xu, H. Yao, P. Bi, L. Hong, J. Zhang, Y. Zu, T. Zhang, J. Qin, J. Ren, Z. Chen, C. He, X. Hao, Z. Wei, J. Hou, *Advanced Mater.* **2021**, 2102420.
3. M. Vasilopoulou, A. Fakharuddin, A. G. Coutsolelos, P. Falaras, P. Argitis, A. R. b. M. Yusoff, M. K. Nazeeruddin, *Chem. Soc. Rev.* **2020**, 49, 4496.
4. J. Shi, X. Xu, D. Li, Q. Meng, *Small* **2015**, 11, 2472.
5. L. Xiong Y. Guo, J. Wen, H. Liu, G. Yang, P. Qin, G. Fang, *Adv. Funct. Mater.* **2018**, 28, 1802757.
6. E. Mosconi, E. Ronca, F. De Angelis, *J. Phys. Chem. Lett.* **2014**, 5, 2619.

7. A. Soultati, A. Fakharuddin, E. Polydorou, C. Drivas, A. Kaltzoglou, M. I. Haider, F. Kournoutas, M. Fakis, L. C. Palilis, S. Kennou, D. Davazoglou, P. Falaras, P. Argitis, S. Gardelis, A. Kordatos, A. Chroneos, L. Schmidt-Mende, M. Vasilopoulou, *ACS Appl. Energy Mater.* **2019**, *2*, 1663.
8. A. Fakharuddin, L. Schmidt-Mende, G. Garcia-Belmonte, R. Jose, I. Mora-Sero, *Adv. Energy Mater.* **2017**, *7*, 1700623.
9. P. Caprioglio, M. Stolterfoht, C. M. Wolff, T. Unold, B. Rech, S. Albrecht, D. Neher, *Adv. Energy Mater.* **2019**, *9*, 1901631.
10. B. Chen, P. N. Rudd, S. Yang, Y. Yuan, J. Huang, *Chem. Soc. Rev.* **2019**, *48*, 3842.
11. Y. Li, Y. Zhao, Q. Chen, Y. (M.) Yang, Y. Liu, Z. Hong, Z. Liu, Y.-T. Hsieh, L. Meng, Y. Li, Y. Yang, *J. Am. Chem. Soc.* **2015**, *137*, 15540.
12. R. Azmi, N. Nurrosyid, S.-H. Lee, M. A. Mubarak, W. Lee, S. Hwang, W. Yin, T. K. Ahn, T.-W. Kim, D. Y. Ryu, Y. R. Do, S.-Y. Jang, *ACS Energy Lett.* **2020**, *5*, 1396.
13. J. Jiang, Z. Jin, J. Lei, Q. Wang, X. Zhang, J. Zhang, F. Gao, S. (F.) Liu, *J. Mater. Chem. A* **2017**, *5*, 9514.
14. R. Sorrentino, E. Kozma, S. Luzzati, R. Po, *Energy Environ. Sci.* **2021**, *14*, 180.
15. L. Lei, S. Yang, Y. Yu, M. Li, J. Xie, S. Bao, P. Jin, A. Huang, *J. Mater. Chem. A* **2019**, *7*, 21085.
16. H. Kanda, O. J. Usiobo, C. Momblona, M. Abuhelaiqa, A. A. Sutanto, C. Igci, X.-X. Gao, J.-N. Audinot, T. Wirtz, M. K. Nazeeruddin, *Solar RRL* **2020**, *5*, 2000650.
17. A. A. Sutanto, R. Szostak, N. Drigo, V. I. E. Queloz, P. E. Marchezi, J. C. Germino, H. C. N. Tolentino, M. K. Nazeeruddin, A. F. Nogueira, G. Grancini, *Nano Lett.* **2020**, *20*, 3992.
18. Z. Jiang, F. Wang, K. Fukuda, A. Karki, W. Huang, K. Yu, T. Yokota, K. Tajima, T.-Q. Nguyen, T. Someya, *PNAS* **2020**, *117*, 6391.
19. L. Fu, H. Li, L. Wang, R. Yin, B. Li, L. Yin, *Energy Environ. Sci.* **2020**, *13*, 4017.

20. E. Polydorou, I. Sakellis, A. Soultati, A. Kaltzoglou, T. A. Papadopoulos, J. Briscoe, D. Tsikritzis, M. Fakis, L. C. Palilis, S. Kennou, P. Argitis, P. Falaras, D. Davazoglou, M. Vasilopoulou, *Nano Energy* **2017**, *34*, 500.
21. J. Zhao, Y. Li, H. Lin, Y. Liu, K. Jiang, C. Mu, T. Ma, J. Y. L. Lai, H. Hu, D. Yu, H. Yan, *Energy Environ. Sci.* **2015**, *8*, 520.
22. L. Hu, Y. Liu, L. Mao, S. Xiong, L. Sun, N. Zhao, F. Qin, Y. Jiang, Y. Zhou, *J. Mater. Chem. A* **2018**, *6*, 2273.
23. Y. Jiang, L. Sun, F. Jiang, C. Xie, L. Hu, X. Dong, F. Qin, T. Liu, L. Hu, X. Jiang, Y. Zhou, *Mater. Horiz.* **2019**, *6*, 1438.
24. Y. Gu, Y. Liu, T. P. Russell, *ChemPlusChem* **2020**, *85*, 751.
25. X. Zhu, L. Hu, W. Wang, X. Jiang, L. Hu, Y. Zhou, *ACS Appl. Energy Mater.* **2019**, *10*, 7602.
26. C.-Z. Li, C.-Y. Chang, Y. Zang, H.-X. Ju, C.-C. Chueh, P.-W. Liang, N. Cho, D. S. Ginger, A. K.-Y. Jen, *Adv. Mater.* **2014**, *26*, 6262.
27. J. Liu, J. Li, X. Liu, F. Li, G. Tu, *ACS Appl. Mater. Interfaces* **2018**, *10*, 2649.
28. S. Woo, W. H. Kim, H. Kim, Y. Yi, H.-K. Lyu, Y. Kim, *Adv. Energy Mater.* **2014**, *4*, 1301692.
29. M. Tountas, A. Verykios, E. Polydorou, A. Kaltzoglou, A. Soultati, N. Balis, P. A. Angaridis, M. Papadakis, V. Nikolaou, F. Auras, L. C. Palilis, D. Tsikritzis, E. K. Evangelou, S. Gardelis, M. Koutsourelis, G. Papaioannou, I. D. Petsalakis, S. Kennou, D. Davazoglou, P. Argitis, P. Falaras, A. G. Coutsolelos, M. Vasilopoulou, *ACS Appl. Mater. Interfaces* **2018**, *10*, 20728.
30. B. R. Lee, H. Choi, J. SunPark, H. J. Lee, S. O. Kim, J. Y. Kim, M. H. Song, *J. Mater. Chem.* **2011**, *21*, 2051.
31. W. Yu, L. Huang, D. Yang, P. Fu, L. Zhou, J. Zhang, C. Li, *J. Mater. Chem. A* **2015**, *3*, 10660.
32. E. Zojer, T. C. Taucher, O. T. Hoffman, *Adv. Mater. Interfaces* **2019**, *6*, 1900581.
33. Q. Chen, C. Wang, Y. Li, L. Chen, *J. Am. Chem. Soc.* **2020**, *142*, 18281.

34. S. A. Ok, B. Jo, S. Somasundaram, H. J. Woo, D. W. Lee, Z. Li, B.-G Kim, J. H. Kim, Y. J. Song, T. K. Ahn, S. Park, H. J. Park, *Nat. Commun.* **2018**, *9*, 4537.
35. N. Boens, B. Verbelen, W. Dehaen, *Eur. J. Org. Chem.* **2015**, 6577.
36. Y. Zhou, C. Fuentes-Hernandez, J. Shim, J. Meyer, A. J. Giordano, H. Li, P. Winget, T. Papadopoulos, H. Cheun, J. Kim, M. Fenoll, A. Dindar, W. Haske, E. Najafabadi, T. M. Khan, H. Sojoudi, S. Barlow, S. Graham, J.-L. Brédas, S. R. Marder, A. Kahn, B. Kippelen, *Science* **2012**, *336*, 327.
37. N. Chakravarthi, U. K. Aryal, K. Gunasekar, H.-Y. Park, Y.-S. Gal, Y.-R. Cho, S. I. Yoo, M. Song, S.-H. Jin, *ACS Appl. Mater. Interfaces* **2017**, *9*, 24753.
38. K.-G. Lim, S. Ahn, T.-W. Lee, *J. Mater. Chem. C* **2018**, *6*, 2915.
39. J. S. Park, J. M. Lee, S. K. Hwang, S. H. Lee, H.-J. Lee, B. R. Lee, H. I. Park, J.-S. Kim, S. Yoo, M. H. Song, S. O. Kim, *J. Mater. Chem.* **2012**, *22*, 12695.
40. T. Yajima, Y. Hikita, M. Minohara, C. Bell, J. A. Mundy, L. F. Kourkoutis, D. A. Muller, H. Kumigashira, M. Oshima, H. Y. Hwang, *Nat. Commun.* **2015**, *6*, 6759.
41. M. Baglan, S. Ozturk, B. Gür, K. Meral, U. Bozkaya, O. A. Bozdemir, S. Atilgan, *RSC Adv.* **2013**, *3*, 15866.
42. M. Zhang, Q. Chen, R. Xue, Y. Zhan, C. Wang, J. Lai, J. Yang, H. Lin, J. Yao, Y. Li, L. Chen, Y. Li, *Nat. Commun.* **2019**, *10*, 4593.
43. G. Lakhwani, A. Rao, R. H. Friend, *Annu. Rev. Phys. Chem.* **2014**, *65*, 557.
44. M. C. Heiber, T. Okubo, S.-J. Ko, B. R. Luginbuhl, N. A. Ran, M. Wang, H. Wang, M. A. Uddin, H. Y. Woo, G. C. Bazan, T.-Q. Nguyen, *Energy Environ. Sci.* **2018**, *11*, 3019.
45. Y. Lin, Y. Firdaus, M. I. Nugraha, F. Liu, S. Karuthedath, A.-H. Emwas, W. Zhang, A. Seitkhan, M. Neophytou, H. Faber, E. Yengel, I. McCulloch, L. Tsetseris, F. Laquai, T. D. Anthopoulos, *Adv. Sci.* **2020**, *7*, 1903419.

46. X. Du, T. Heumueller, W. Gruber, O. Almora, A. Classen, J. Qu, F. He, T. Unruh, N. Li, C. J. Brabec, *Adv. Mater.* **2020**, *32*, 1908305.
47. A. Soultati, A. Verykios, S. Panagiotakis, K.-K. Armadorou, M. I. Haider, A. Kaltzoglou, C. Drivas, A. Fakharuddin, X. Bao, C. Yang, A. R. b. M. Yusoff, E. K. Evangelou, I. Petsalakis, S. Kennou, P. Falaras, K. Yannakopoulou, G. Pistolis, P. Argitis, M. Vasilopoulou, *ACS Appl. Mater. Interfaces* **2020**, *12*, 21961.
48. E. A. Alharbi, A. Y. Alyamani, D. J. Kubicki, A. R. Uhl, B. J. Walder, A. Q. Alanazi, J. Luo, A. Burgos-Caminal, A. Albadri, H. Albrithen, M. H. Alotaibi, J.-E. Moser, S. M. Zakeeruddin, F. Giordano, L. Emsley, M. Grätzel, *Nat. Commun.* **2019**, *10*, 3008.
49. S. Wang, A. Wang, X. Deng, L. Xie, A. Xiao, C. Li, Y. Xiang, T. Li, L. Ding, F. Hao, *J. Mater. Chem. A* **2020**, *8*, 12201.
50. Y. Pei, Y. Liu, F. Li, S. Bai, X. Jian, M. Liu, *iScience* **2020**, *15*, 165.
51. G. Grancini, C. Roldán-Carmona, I. Zimmermann, E. Mosconi, X. Lee, D. Martineau, S. Narbey, F. Oswald, F. De Angelis, M. Graetzel, M. K. Nazeeruddin, *Nat. Commun.* **2017**, *8*, 15684.
52. J. Yuan, Y. Zhang, L. Zhou, G. Zhang, H.-L. Yip, T.-K. Lau, X. Lu, C. Zhu, H. Peng, P. A. Johnson, M. Leclerc, Y. Cao, J. Ulanski, Y. Li, Y. Zou, *Joule* **2019**, *3*, 1140.
53. J. Tong, Z. Song, D. H. Kim, X. Chen, C. Chen, A. F. Palmstrom, P. F. Ndione, M. O. Reese, S. P. Dunfield, O. G. Reid, J. Liu, F. Zhang, S. P. Harvey, Z. Li, S. T. Christensen, G. Teeter, D. Zhao, M. M. Al-Jassim, M. F. A. M. van Hest, M. C. Beard, S. E. Shaheen, J. J. Berry, Y. Yan, K. Zhu, *Science* **2019**, *364*, 475.

Table 1 Summary of the performance characteristics of OSCs based on MP6:IT-4F absorber with different BDPs as efficiency stabilizers. The J_{sc} values calculated from EQE curves are also included.

	J_{sc} (mA cm ⁻²)	$J_{sc-calc}$ (mA cm ⁻²)	V_{oc} (V)	FF	PCE (%)	R_s (Ω cm ²)
w/o BDP	20.10	19.60	0.81	0.68	11.08	2.3
DiTertButyl- BDP	20.97	19.23	0.86	0.72	12.98	1.3
DTB-pH- BDP	19.15	19.03	0.82	0.68	10.68	2.6
BDP-NO ₂	18.15	18.17	0.82	0.64	9.53	5.4
BDP-COOH	19.34	19.26	0.82	0.69	10.94	1.7
BDP-O- triple	20.48	20.40	0.84	0.69	11.87	2.4

BDP-NH ₂	21.54	21.20	0.87	0.74	13.87	1.1
BDP-COOCH ₃	19.51	20.07	0.84	0.70	11.82	1.9
BDP-OH	20.96	20.00	0.86	0.72	12.97	1.4
DoH-BDP	20.02	20.26	0.84	0.68	11.44	2.6

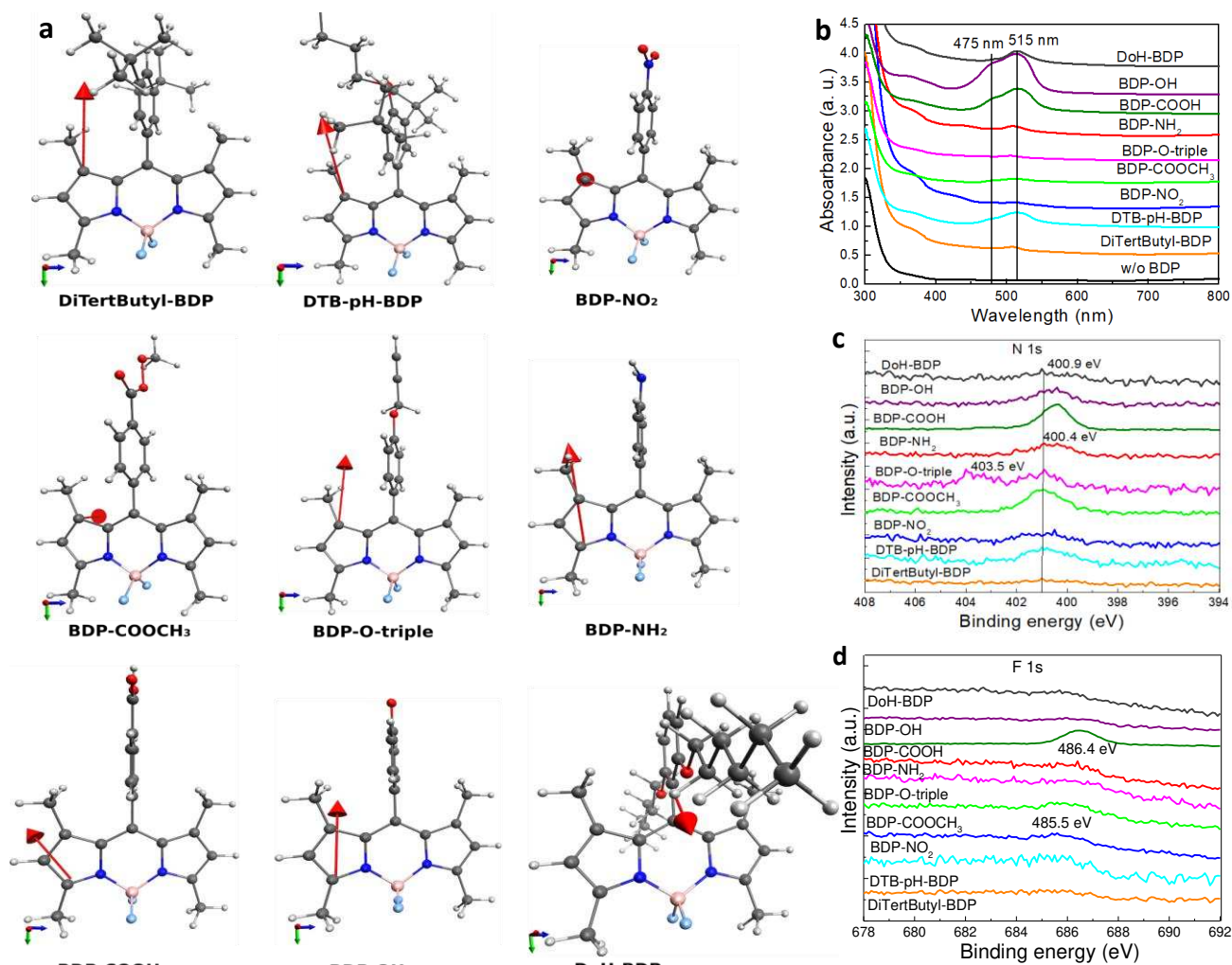


Figure 1. Structural and optical properties of BDPs. (a) Optimized structures for the BDP molecules at the B3LYP/6-31+G(d,p) level of theory in gas phase. C/N/B/F/H atoms in grey / blue / pink / light blue / white colours. The reference Cartesian axis is also shown (red / blue / green corresponds to x / y / z axis), together with the total dipole moment vector (red arrow, see Table S2 for the computed values). (b) UV-Vis absorption spectra of ZnO layers either pristine or coated with BODIPYs from their respective methanol solutions with a concentration of 1 mg mL⁻¹. (c) N 1s and (d) F 1s core level XPS peaks of ZnO layers coated with different BODIPYs.

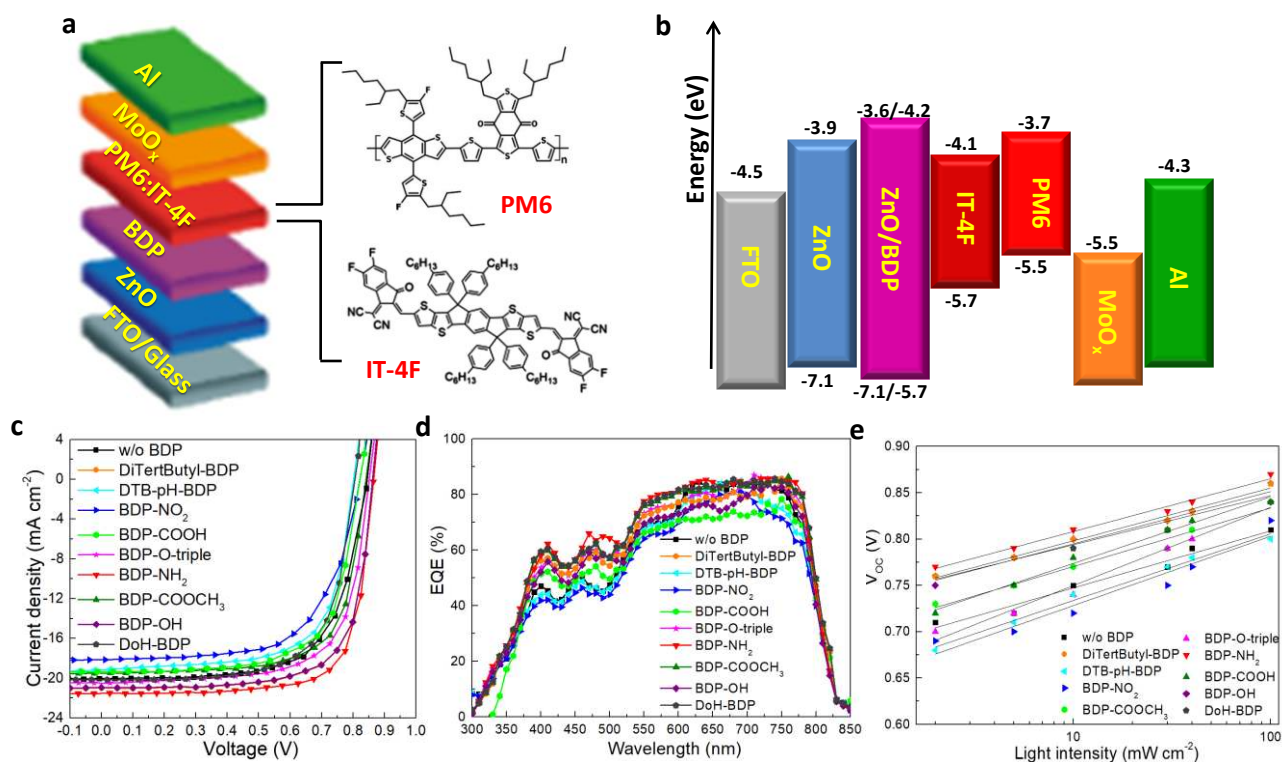


Figure 2. Organic solar cells performance. (a) The device architecture and the chemical structures of PM6 donor and IT-4F acceptor used in the organic absorber. (b) Energy levels of the different device layers considering vacuum level alignment before contact. For FTO and Al electrodes as well as for ZnO (pristine and coated with BDPs) and MoO_x electron and hole transporting layer, respectively, the W_F values are denoted (for ZnO the valence band edge is also shown). For polymer donor and non-fullerene acceptor the HOMO, LUMO levels are shown. (c) Current density-voltage (J-V) characteristics and (d) EQE spectra of PM6:IT-4F based OSCs with pristine and coated with different BDPs ZnO electron transporting layer. (e) Variation of open-circuit voltage (V_{oc}) versus light intensity (ranging between 2 and 100 mW cm⁻²) of the OSCs with different BODIPY interlayers.

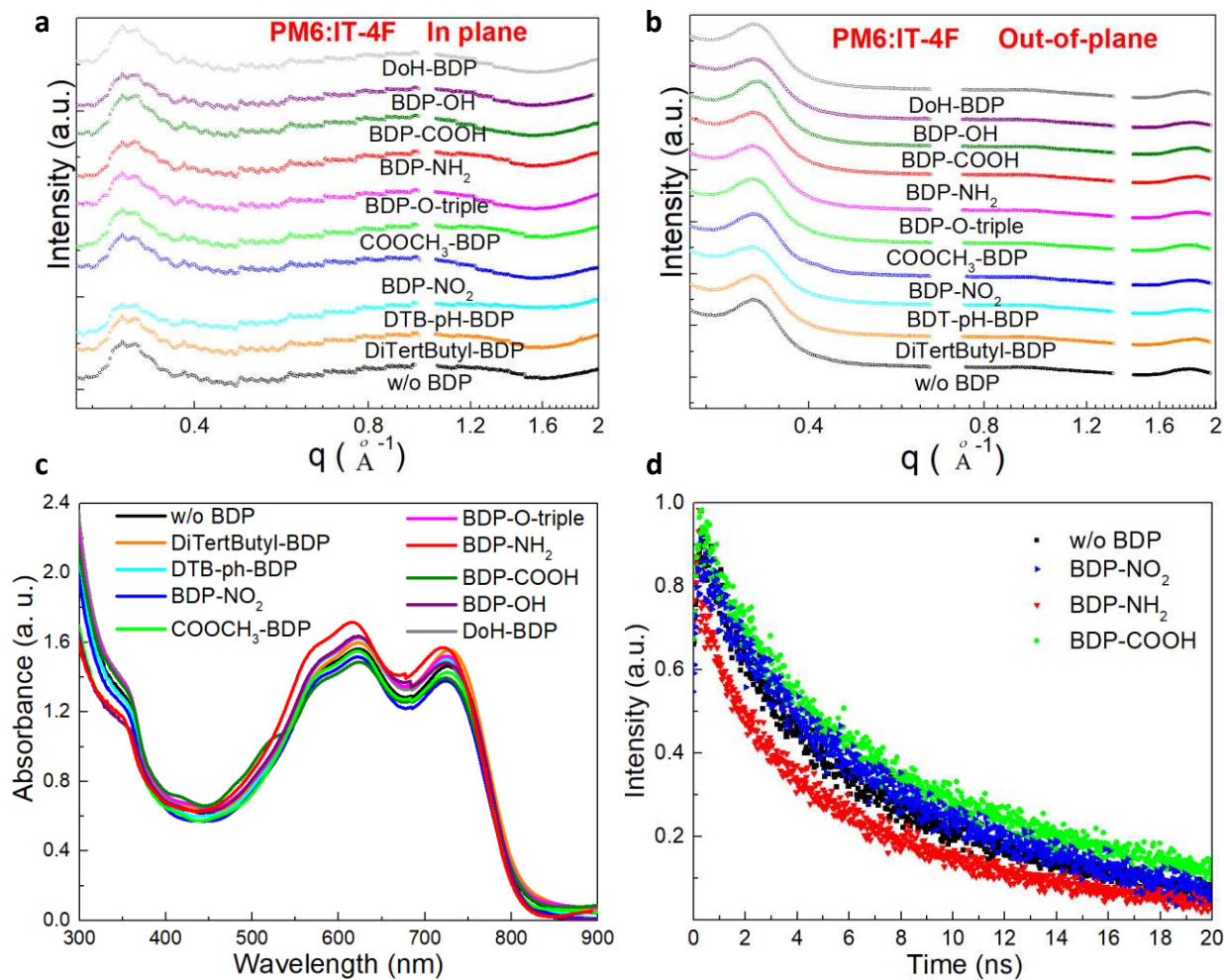


Figure 3. Morphology of the organic absorber. The GIWAXS intensity profiles along the (a) out-of plane and (b) in-plane directions of PM6:IT-4F blend film deposited on different ZnO substrates. (c) UV-Vis absorption of PM6:IT-4F films (of the same thickness) deposited on pristine and coated with different BDPs ZnO. (d) Transient PL decay rates of PMY:IT-4F blend film deposited on pristine ZnO and ZnO coated with three different representative BODIPYs.

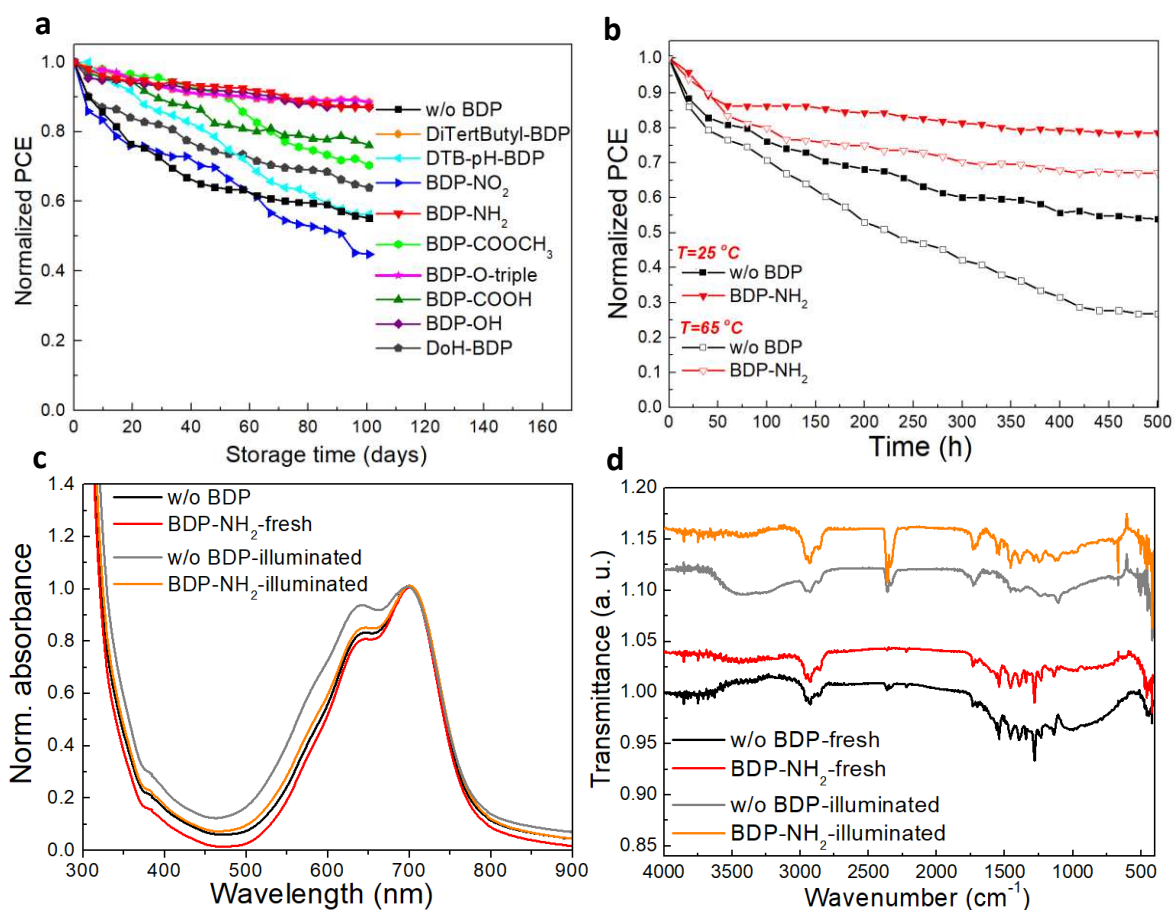


Figure 4. Stability tests. (a) Long-term stability of OSCs using ZnO ETLs w/o and with different BDP coatings. The devices were kept/measured in nitrogen and stored in the dark between measurements. (b) Variation of PCE versus time of constant 1 sun illumination of OSCs using either pristine or BDP-NH₂ coated ZnO ETLs. The devices were tested in nitrogen at two different temperatures, in particular, 25 °C and 65 °C. Changes upon UV irradiation for 10 hours in the (c) normalized absorption and (d) FTIR spectra of IT-4F films coated on ZnO substrate either pristine or coated with BDP-NH₂.

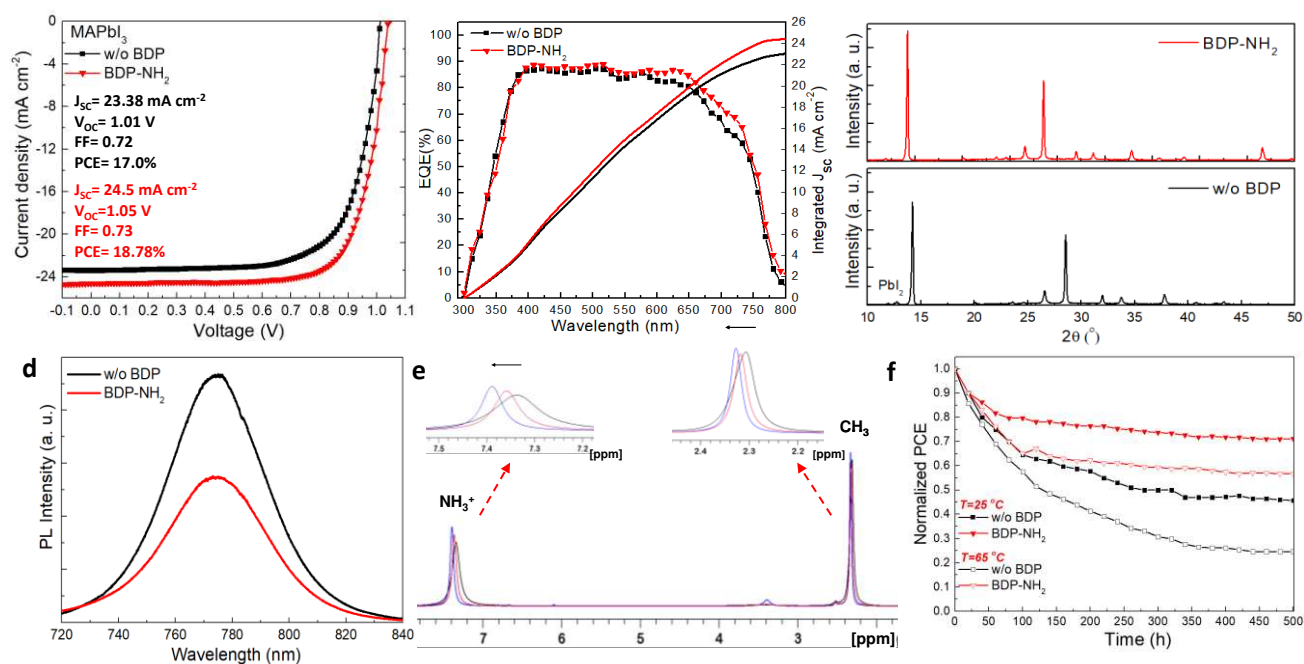


Figure 5. Perovskite solar cells. (a) Reverse scan J-V characteristics under AM 1.5G illumination of the best performing PSCs using SnO₂ ETLs either pristine (w/o BDP) or coated with BDP-NH₂ and (b) IPCE spectra and integrated J_{sc} of the same cells. (c) XRD patterns of fresh MAPbI₃ perovskite films grown on SnO₂/FTO substrates w/o and with BDP-NH₂ coating. (d) Steady-state PL spectra of MAPbI₃ films grown on SnO₂/FTO substrates w/o and with BDP-NH₂ coating. The inset shows the PL spectra of the perovskite films grown on glass substrates w/o and with BDP-NH₂ coating. (e) Partial ¹H NMR spectra (500 MHz, DMSO-d₆, 298.0 K) of CH₃NH₃ in MAPbI₃ (2.8 M) before and after addition of BDP-NH₂ (stock solution 69.28 mM). (f) Variation of PCE versus time of constant 1 sun illumination of PSCs using either pristine or BDP-NH₂ coated SnO₂ ETLs. The devices were tested in nitrogen at two different temperatures, in particular, 25 °C and 65 °C.

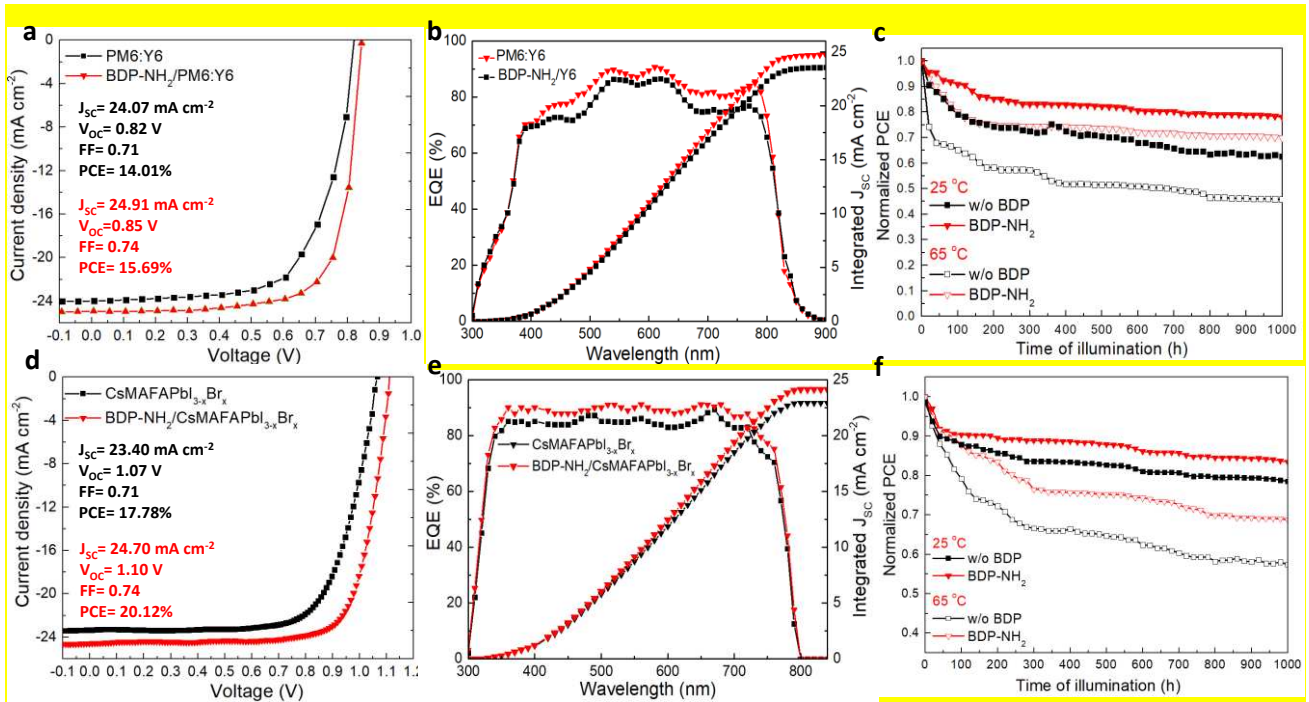


Figure 6. The universality of BDP-NH₂ interlayer. (a) J-V characteristic curves taken under 1.5 AM illumination and (b) EQE spectrum of OSCs based on PM6:Y6 absorber and BDP-NH₂ interlayer. (c) Reverse scan J-V characteristic curves taken under 1.5 AM illumination and (d) EQE spectrum of PSCs based on Cs_{0.05}FA_{0.8}MA_{0.15}PbI_{2.55}Br_{0.45} absorber and BDP-NH₂ interlayer. (e) Stability studies of both OSCs and PSCs under continuous illumination (in nitrogen) without and with heating (at 65 °C) for 1000 h.